Journal of Energy Chemistry 66 (2022) 168–180

Contents lists available at ScienceDirect

Journal of Energy Chemistry

journal homepage: www.elsevier.com/locate/jechem

http://www.journals.elsevier.com/journal-of-energy-chemistry/

PtRu nanoparticles supported on noble carbons for ethanol electrooxidation

Alberto Rodríguez-Gómez [a,1], Enrico Lepre [b,1], Luz Sánchez-Silva [a], Nieves López-Salas [b], Ana Raquel de la Osa [a,*]

[a] Faculty of Chemical Sciences and Technologies, University of Castilla-La Mancha, Enrique Costa Novella Building. Avda. Camilo Jose Cela, 12, 13071 Ciudad Real, Spain
[b] Colloid Chemistry Department, Max Planck Institute of Colloids and Interfaces, Am Mühlenberg 1, 14476 Potsdam, Germany

ARTICLE INFO

Article history:
Received 25 March 2021
Revised 30 June 2021
Accepted 7 July 2021
Available online 16 July 2021

Keywords:
Noble carbon
Cytosine
H_2 production
Ethanol electrooxidation
PtRu anode
PEM cell

ABSTRACT

In this work, three cytosine derived nitrogen doped carbonaceous materials (noble carbons, NCs) with different atomic C/N ratios and porous networks have been synthesized and used as supports for PtRu electrocatalysts in the ethanol oxidation reaction (EOR) for clean hydrogen production. Both, the metal phase and the carbon support play critical roles in the electrocatalysts final performance. Lower NPs size distribution was obtained over supports with low atomic C/N ratios (i.e., 4 and 6) and defined porosity (i.e., 1701 $m^2 g^{-1}$ for PtRu/CNZ and 1834 $m^2 g^{-1}$ for PtRu/CLZ, respectively). In contrast, a lower C/N ratio and poor porous network (i.e., 65 $m^2 g^{-1}$, PtRu/CLK) led to the largest particle size and fostered an increase of the alloying degree between Pt and Ru NPs (i.e., 3% for C/N ~ 6 and 28% for C/N ~ 3). Electrochemical active surface area was found to increase with decreasing NPs size and the alloy extent, due to a higher availability of Pt active sites. Accelerated degradation tests showed that PtRu/NCs outperform similar to PtRu NPs on commercial carbon pointing at the stabilizing effect of NCs. PtRu/CNZ exhibited the best electrochemical performance (i.e., 69.1 mA mg_{Pt}^{-1}), outperforming PtRu/CLZ and PtRu/CLK by 3- and 9-fold, respectively, due to a suitable compromise between particle sizes, degree of alloy, textural properties and elemental composition. Best anodes were scaled-up to a proton exchange membrane cell and PtRu/CNZ was proved to provide the best electrocatalytic activity (262 mA cm^{-2} and low energy requirements), matching the values obtained by the state of the art of EOR electrocatalysts.

1. Introduction

Ethanol is becoming a promising alternative in replacing several conventional sources of energy due to its convenience in storage, reduced environmental impact and versatile nature. Currently, the production of hydrogen through ethanol electrolysis cells (EECs) is considered an interesting energy vector [1,2]. However, the relatively slow kinetics of the ethanol oxidation reaction (EOR) requires the use of precious metal-base electrocatalysts. In this sense, Pt is well known as the best material for alcohol electrooxidation at low temperature [3]. However, a secondary metal such as Ru, Sn, Mo, Rh or Pb is usually introduced as alloying metal which provides higher electrocatalytic activity and stability of the system, due to the bifunctional effect and the electronic interaction between both metals. In addition, pure Pt can be easily poisoned by CO-containing species strongly adsorbed on the catalyst surface [4]. On the other hand, the chemical nature of the catalytic support is postulated as a key aspect in the electrocatalyst synthesis, since it could improve the nanoparticles properties (size and dispersion) and hence, the electrochemical performance. Accordingly, different materials are currently being investigated to enhance the activity of bimetallic catalysts towards EOR process. Carbon-based supports (commonly carbon black and Vulcan XC-72) are used to maximize the noble metal utilization and reduce costs [5–8]. In this context, the effect of carbon nanofiber [9], TiO_2-embedded carbon nanofibers [10], carbon ceramic electrodes (CCE) [11], low-density carbon nanofibers (CNF f-LS) [2] or even modified few-walled carbon nanotubes (FWCNT) [12] as support for Pt-based nanoparticles on alcohols electrooxidation has also been evaluated. It was concluded that the pore volume of carbon nanofibers plays an important role in the EOR activity. In addition, the interaction between the metal and the support affects not only the reaction kinetics, but also the reaction mechanism, providing less sensitivity to poisoning from adsorbed CO species on the electrocatalyst

* Corresponding author.
E-mail address: AnaRaquel.Osa@uclm.es (A.R. de la Osa).
[1] These authors contributed equally.

https://doi.org/10.1016/j.jechem.2021.07.004

surface. Furthermore, the interactions between the support and the ionomer in the catalyst layer are important in forming a suitable pore structure for an efficient mass transfer, enhancing the electrocatalytic activity. In this sense, aspects such as the available surface area, the pore size distribution or the elemental composition of the carbonaceous support could be essential in order to achieve a suitable active phase deposition.

Among all carbon-based materials, the concept of noble carbon (NC) was introduced by Oschatz et al. [13] in 2018. In brief, the heat treatment of organic compounds, characterized by high heteroatom content and resistance upon oxidation, leads to the formation of even more stable (upon oxidation) carbonaceous materials since only a restricted number of new bonds can be formed due to the release of CO_2, H_2O and NH_3. Ionic liquids, dyes and nucleobases were proposed as candidates to prepare such noble carbonaceous materials. Among them, nucleobases withstand for their large initial heteroatom content (e.g., C/N ratios between 1 and 2) and their natural origin [14]. Previous studies using nucleobases as carbonaceous precursors have shown that such large C/N ratios persist even when carbonaceous materials are prepared from them at high temperatures using salt melt templates. Moreover, composition and pore network can be extensively tuned by varying the carbonization temperature and salt mix used [15,16]. Interestingly, having a highly porous and stable upon oxidation N-doped carbonaceous network is of great interest for Pt-nanoparticle decoration toward ethanol electrooxidation. For instance, local electron density changes induced by nitrogen heteroatoms may lead to the stabilization of nanoparticles and the resistance upon oxidation might induce long-term stability to the overall material [17,18]. However, the possible application of these materials as an electrocatalytic support for ethanol electrolysis has not been explored in the current literature yet.

Herein, we report the preparation of PtRu nanoparticles decorated NC materials obtained from cytosine. Carbonaceous supports were prepared using LiCl/$ZnCl_2$, NaCl/$ZnCl_2$ and LiCl/KCl salt mixes as structure directing agents. The influence of the template agent in the final porous network architecture, nitrogen content and functionalities is discussed and correlated with the morphology and composition of PtRu nanoparticles, obtained after decorating the carbonaceous materials using the polyol-modified method [19]. Finally, the performance of these materials as anodes for ethanol electrochemical oxidation was studied in both, half-cell and proton exchange membrane (PEM) cell configurations, in order to properly explore the electrocatalytic activity towards clean hydrogen production.

2. Experimental section

2.1. Synthesis of noble carbon supports

In a standard procedure, 2 g of cytosine (99%) was mixed in an Agatha mortar with 20 g of LiCl (98%, Sigma Aldrich) and 20 g of $ZnCl_2$ (Merck). The solid mixture was submitted to heat treatment in N_2 atmosphere at 800 °C for 2 h using 1 °C min g^{-1} heating ramp. After spontaneous cooling down a grey foam was obtained. The sample was washed two times at room temperature over night with 0.5 L of 1 M HCl (Roth) aqueous solution and one more time at 50 °C with 150 mL HCl 1 M. The solid product was filtered under vacuum and dried at 70 °C for 5 h at atmospheric pressure and at 150 °C overnight in a vacuum oven (5 mbar). The final product was obtained with 30% of yield and it appeared as a black fluffy powder. The obtained sample was named as CLZ where 'C' stands for cytosine, 'L' stands for lithium chloride and 'Z' stands for zinc chloride.

The same procedure described for CLZ was followed to prepare CNZ and CLK samples, where 'N' stands for sodium chloride (98%, Sigma Aldrich) and 'K' stands for KCl. Then, in a standard CNZ synthesis, 2 g of cytosine, 20 g of $ZnCl_2$, and 20 g of NaCl were used as precursor and templating agent for the material. CLK samples were prepared by mixing 2 g of cytosine with 24 g of LiCl and 16 g of KCl. Both, CNZ and CLK were treated identically as CLZ thereafter.

2.2. Synthesis of PtRu/NC anodes

PtRu/NC electrocatalysts (60 wt% and 2:1 of mass ratio) were synthetized using the modified polyol method. In a typical procedure, appropriate amounts of hexachloroplatinic acid ($H_2PtCl_6 \cdot xH_2O$, Alfa Aesar) and ruthenium choired ($RuCl_3$, Alfa Aesar) were dissolved in 50 mL of ethylene glycol (99%, Sigma Aldrich). In order to ensure the nanoparticles formation, 0.4 g of NaOH (99.8%, Panreac) was added to the bulk solution and the mixed was stirred at ambient conditions for 1 h. Subsequently, the temperature was increased to 190 °C for 2 h, taking place the co-reduction of the mixed salts forming Pt-Ru nanocolloids. After the reduction step, the noble carbon support (CNZ, CLZ or CLK) was added to the bulk solution, which was cooled down to room temperature and stirred for 48 h. Finally, the resulted slurry was filtered, washed with distilled water, and the precipitate was dried in an oven at 80 °C overnight.

2.3. Physicochemical characterization

The crystallinity of the electrocatalysts was determined by X-ray diffraction (XRD) analyses. The XRD experiments were conducted with a Philips X'Pert instrument using nickel-filtered Cu K_α radiation. Samples were scanned at a rate of 0.02° $step^{-1}$ within the range $5° \leq 2\theta \leq 90°$ (scan time = 2 s $step^{-1}$). Bruker D8 Advance instrument with Cu-K_α radiation source (λ = 0.154 nm) and NaI scintillation counter-Scinti-Detector was used to record powder XRD. The diffraction patterns were obtained in the 2θ range between 5°–70° with steps of 0.05° and 2 s. A Thermo Microbalance TG 209 F1 Libra (Netzsch, Selb, Germany) was used to perform thermogravimetric analysis (TGA) using either nitrogen or synthetic air as carrier gas (20 cm^3 min^{-1}) and a heating rate of 10 K min g^{-1} in a Pt crucible. In a typical analysis, 0.01 g of sample was analyzed.

Inductively coupled plasma optical emission spectrometry (ICP-OES) measurements were conducted with a PerkinElmer ICP-OES Optima 8000. In a standard procedure before ICP-OES measurements, samples (0.01 g) were dissolved in 500 μL of 1:2 mixture of concentrated HNO_3 and HCl, the heterogeneous mixture was kept at room temperature for 12 h, at 96 °C for 1 h. The digested samples were then brought to 10 mL using ultrapure water and filtrated before the measure. Four calibration standard solutions per element were used to obtain a calibration curve. All the samples were measured in triplicate and the values given in the manuscript are average values. LEO 15550-Gemini instrument from Zeiss was used to record scanning electron microscopy (SEM) after sputtering samples with ca. 10 nm layer of a 80% gold/20% platinum mixture. Energy-dispersive X-ray (EDX) spectroscopy was run using a couple EDX analyzer (Oxford instruments). Transmission electron microscopy (TEM) was performed in an EM 912 Zeiss instrument operating at 120 kV. TEM grids were prepared by drop casting carbon coated copper grids with ethanol dispersions of the samples. Quantachrome Quadrasorb SI apparatus was used to carry out nitrogen adsorption and desorption isotherms at 77 K and carbon dioxide adsorption and desorption isotherms at 273 K. Before each measurement, samples were degassed at 150 °C under vacuum (0.5 Torr) for 20 h using a 3P instruments Masterprep degassing machine. Specific surface area was calculated from nitrogen adsorption data (P/P_0 < 0.2) using the Brunauer-Emmett-Teller (BET) method. Total pore volume (V_T) was calculated from the amount of nitrogen or carbon dioxide adsorbed at P/P_0 = 0.995. Quenched solid density functional theory (QSDFT) model with

slit/cylindrical pore shape was used to calculate the pore size distribution using nitrogen adsorption branch at 77 K. Non-local density functional theory (NLDFT) was applied to the adsorption branch of CO_2 isotherms at 273 K to obtain the pore size distribution of the samples. Temperature programmed reduction (TPR) experiments were conducted in a commercial Micromeretics AutoChem 2950 HP unit with TCD detection. Samples (ca. 0.08 g) were loaded into a U-shaped tube and ramped from room temperature to 900 °C (10 °C min^{-1}), using a reducing gas mixture of 5 vol% H_2/Ar (60 NmL min^{-1}).

2.4. Electrochemical characterization in a half-cell system

Electrochemical measurements were conducted at room temperature in a conventional three-electrodes glass cell with a potentiostat/galvanostat instrument (PPGTAT128N Ecochemie, Netherlands) controlled by the software Autolab (Nova 2.1). The counter electrode was a platinum foil while Ag/AgCl electrode (saturated in 3 M KCl, Metrohm) was used as a reference. The working electrode consisted in a glassy carbon rotating disk (GC-RDE, Metrohm Autolab) of 0.19 cm^2 of active area (diameter of 5 mm). All the potential values are referred to the reversible hydrogen electrode (RHE) according to the Nernst equation. Catalyst ink was prepared as follows: 2 mg of catalyst powder was dispersed in 0.75 mL of 2-propanol (99.9 %, Sigma-Aldrich), 0.25 mL of deionized water and 8 μL of a Nafion solution (5 wt%, Sigma-Aldrich) by sonication for 30 min. A 10 μL aliquot of the catalyst ink was deposited on the glassy carbon tip reaching a total metal loading of 0.063 mg cm^{-2}. Subsequently, the electrode was dried in air at room temperature for 2 h. Prior to each electrochemical measurement, the surface of the working electrode is polished with an aluminum oxide slurry (grain size 0.3 μm) and washed with Mili-Q water.

The characterization of the as-synthesized materials was carried out by cyclic voltammetry (CV) tests with a 0.5 M $HClO_4$ (Scharlau) electrolyte in a potential interval from − 0.068 to 1.36 V vs. RHE at a scan rate of 50 mV s^{-1}. Reported voltammograms correspond to the 20th cycle to achieve a stable profile. The electrochemical active surface area (ECSA) was determined from the peaks in the hydrogen adsorption/desorption region of the CV profiles. In addition, an accelerated durability test (ADT) was carried out in order to analyze the electrocatalysts stability, repeating the CV essays for 500 cycles at the same conditions mentioned above. The degradation degree was estimated by the ECSA losses between first and last cycle. Thereafter, the electrochemical activity toward the EOR was evaluated in 4 M EtOH with different $HClO_4$ concentrations (0.004 and 0.5 M) by applying a potential interval from − 0.2–1.2 V vs. RHE at a scan of 10 mV s^{-1}. All solutions were deaerated by bubbling N_2 for 20 min and then the inert atmosphere was maintained over the solution during test. Also, the working electrode was rotated at 100 r min^{-1} in order to achieve a homogenous and uniform catalyst film. The anti-poison ability of PtRu/NCs was explored through CO-Stripping essays. Prior to the test, CO was introduced for 20 min to ensure the adsorption on the catalyst surface. After CO saturation, a stream of N_2 was bubbled to eliminate the excess of CO in the electrolyte. CV profiles were then obtained from a potential range of 0 to 1.2 V vs. RHE at 20 mV s^{-1}. Finally, to evaluate the stability, a long-term galvanostatic test was carry out at a fixed current density of 1 mA cm^{-2} for 10 h. An optical microscope (MOTIC DMW B1-223-ASC) was used in order to examine possible changes in the catalytic layer deposited on the glassy carbon tip before and after the chrono- test.

2.5. Electrochemical reforming essays in a PEM cell

Electrochemical reforming measurements were carried out in a PEM electrolysis cell SQUAREPARK 5 (Pragma industries) with a geometric surface area of 5 cm^2 described in detail elsewhere [20]. The membrane electrode assembly (MEA) consisted of a proton exchange membrane (Nafion 117, Hidrógena S.A.) and two working electrodes (anode and cathode). A commercial Pt supported on carbon black catalyst (20 wt%, Alfa Aesar) was used as the cathode, while the different pre-synthesized PtRu/NC (60 wt %) was used as the anode. Coating inks were prepared with proper amounts of each powder catalyst and a Nafion aqueous solution (binder/catalyst ratio of 3.64) dissolved in 2-propanol in order to achieve a total metal loading of 0.5 and 1.5 mg cm^{-2} for the cathode and anode, respectively. Inks were deposited directly on both sides of the membrane by spraying at 80 °C with no need of assembly. A previous work has shown that such configuration enhances the electrochemical performance [21]. The gas diffusion layer (GDL) was carbon paper TGP-H90 (Fuel Cells Earth) of 5 cm^2 and 0.1 mm of thickness. The cell was operated at 80 °C with a 4 M ethanol solution supplied to the anodic chamber (1.15 mL min^{-1}) while deionized water was fed to the cathodic compartment (1.6 mL min^{-1}) operating in a continuous mode. Both streams were preheated at 80 °C and the flow rates were regulated using a multichannel peristaltic pump (5001, Heidolph). Also, with the purpose of avoiding ethanol evaporation, a cooling condensation column was installed in the anodic reservoir (−5 °C).

Electrochemical measurements were carried out using a potentiostat/galvanostat VERTEX 5 V (Ivium Technology) controlled by a research electrochemistry software. In order to study the electrocatalytic performance in a preliminary way, linear sweep voltammetry (LSV) tests were carried out in a potential range between 0–1.4 V and 20 mV s^{-1} of scan rate. Stationary measurements (chronopotentiometry) were performed applying different levels of constant current from 0.2 to 0.6 A at intervals of 0.2 A, maintaining each level for 900 s. Reaction products flow rates were quantified and the total ethanol conversion was estimated for each applied current step. The organic compounds derived from the ethanol electro reforming process were analyzed in an Agilent Technologies 8220 A gas chromatograph (offline mode) equipped with a FID detector and a capillary column (Agilent DB-WAS UI, 30 m × 0.2 mm × 0.25 μm), using helium as a carrier gas. Hydrogen production flow rate was measured by a high-precision flowmeter (Mervilab) and was also compared with the theoretical predicted by the Faraday's law.

3. Results and discussion

3.1. Synthetic method and operating conditions

Cytosine nucleobases (C/N ratio of 1.1) was chosen as a model noble carbonaceous precursor since it shows ca. 30% of residual mass after direct carbonization at 900 °C in nitrogen atmosphere [22]. Indeed, it is not a trivial issue since large yields are usually ascribed to polymeric carbon precursors. When carbonizing molecular precursors, such large yields were obtained using molecular precursors containing polymerizable functional groups (e.g., cyanogroups) [23]. Large surface area carbonaceous materials were prepared using inorganic salts melts as structure directing agents. Salts melt templating strategy is a well-established method to produce highly porous materials [24]. In brief, a mix of two inorganic salts (e.g., $ZnCl_2$ and LiCl) is prepared and mixed with the desired organic precursor. The mixture is then submitted to heat treatment and, upon increasing the temperature, the salt mix melts. Given the melting occurring before the condensation of the organic precursor upon carbonization starts, after cooling down and acid washing of the resulting cake, a porous powdered carbonaceous material is obtained. It is known that changing the composition of the inorganic mixes different heteroatom doping and porosities can be

obtained [24]. Herein, we used LiCl/$ZnCl_2$ 1/1 wt% (LZ), NaCl/$ZnCl_2$ 1/1 wt% (NZ) and LiCl/KCl 3/2 wt% (LK) as structure directing salt mixes for cytosine. Cytosine was blended together in a 1:20 w/w ratio with the different salts. Subsequently, it was submitted to heat treatment at 800 °C for 2 h. The materials obtained after cooling down and acid washing the samples will be named hereafter as CLZ, CNZ and CLK, respectively. Those materials were subsequently used as supports of PtRu nanoparticles using the modified-polyol method. Hereafter, the synthetized PtRu/NC electrocatalysts are denoted as PtRu/CNZ, PtRu/CLZ and PtRu/CLK depending on the noble carbon support used.

3.2. Physicochemical characterization

The elemental chemical composition of the noble carbon supports before active phase deposition was evaluated through EDX and ICP analysis (Table S1 from the supplementary information). EDX of the substrates revealed that, despite the similarities of the synthesis of CLZ, CNZ and CLK, the samples exhibit different nitrogen contents (i.e., 14 wt%, 19 wt% and 27 wt%, respectively). Interestingly, all the samples exhibit a very large amount of nitrogen heteroatoms which make the surface of the material more polar (i.e., enhancing their wettability) and make them more resistance towards oxidation [25,26]. Also, residual zinc amounts (0.8 wt%) were found after washing all samples (see Table S1, ICP). XPS of the carbonaceous materials (Fig. 1) helped understanding the influence of using different salt melts for the preparation of the materials.

Deconvolution of high resolution XPS N1 *s* peaks shows that all samples comprise components centered at 397, 399, 401 and 403 eV herein ascribed to C–N = C nitrogen atoms, pyrrolic-N, C–N–H uncondensed amino (–NH_2) groups or quaternary-N species and π–π* interactions [27]. From CLZ to CNZ to CLK, the contribution of the peak ascribed to C–N = C nitrogen atoms increases while that ascribed to pyrrolic-N decreases, which goes along with the increase of concentration of nitrogen observed in the same trend. The decrease in the pyrrolic-N sample and the striking intensity of the π–π* band in CNZ indicates that the samples have a larger degree of order than CLZ. The deconvolution of CLZ and CLK C1 *s* peaks in Fig. S1 shows bands centered at 284.7, 285 and 287 eV ascribed to sp^2 C–C bonds, C–N and C–O motifs. The fit of C1 *s* peak of CNZ also shows one motif at 291 eV that is ascribed to π–π* interactions. The metal amounts of the different PtRu/NC catalysts were checked through ICP and EDX (see Table S2 and Fig. S2) confirming a total loading close to 60 wt% and 2:1 of mass ratio between Pt and Ru for all cases.

XRD patterns obtained for the synthesized materials before and after the Pt-Ru active phase deposition are shown in Fig. S3 and Fig. 2, respectively. CLZ and CNZ showed very similar profiles, characterized by a graphitic stacking diffraction peak centered at 26° with very low intensity, suggesting the predominance of an amorphous phase in the materials. Unlike CLZ and CNZ, CLK reflections show a more intense peak at 26° indicating that $ZnCl_2$ contained in the salt mix plays a catalytic role in the carbonization process hindering the formation of graphitic stacks [28]. Regarding the diffraction patterns after metals deposition, no peaks associated with oxidized species (Pt_xO_y or Ru_xO_y) are registered in the obtained profiles. Nevertheless, its presence should not be ignored since they could be found in very small quantities not detectable by XRD technique. In general terms, all PtRu/NC catalysts show a typical face centered cubic (fcc) structure of polycrystalline Pt (Fig. 2), with distinct diffraction peaks at 39°, 46°, 67° and 81° attributed to (1 1 1), (2 0 0), (2 2 0) and (3 1 1) planes, respectively [29–31]. According to the available literature [32,33], characteristic peaks of metallic Ru seem to appear at 38.4°, 42.2° and 44° 2θ angles (JCPDS: 06–663), which hinders their proper identification due to an overlap with the Pt signal. In addition, the absence of Ru peaks could be attributed to other factors such as the formation of PtRu alloy or even to the possible deposition in amorphous form [34]. In this regard, diffraction peaks of all PtRu/NC electrocatalysts are slightly shifted to higher angles compared to the position of pure Pt (dashed lines), indicating the incorporation of Ru atoms into the Pt fcc lattice with the consequent Pt-Ru alloy formation [35,36]. Such effect is more noticeable for PtRu/CLK, leading to a considerably reduction of the lattice constant. Vergard's law ($l_{PtRu} = 0.3913 - 0.012x_{Ru}$) was applied to obtain the alloy formation degree [37], while Scherrer's equation was used to calculate the average particle size from the (2 2 0) Pt peak [38]. Main results are summarized in Table 1. Generally, all electrocatalysts present particle sizes between 5–9 nm, being smaller for PtRu/CNZ (5.2 nm) followed by PtRu/CLZ and PtRu/CLK, which present a higher particle agglomeration grade (9 nm). Regarding the alloy degree, CNZ and CLZ based materials achieve similar results (around 3%–5%), while CLK support seems to promote the alloy formation (up to 28%). Bearing in mind that the Pt-Ru content is the same for all the synthesized electrocatalyst, such variations (particle size and alloy degree) may be ascribed to the interactions between PtRu nanoparticles and the different noble carbon supports, and/or the physicochemical properties of these latter.

Scanning and transmission electron micrographs (SEM and TEM) of CLZ, CNZ and CLK and the correspondent PtRu/NC samples were obtained to get better understanding of all materials morphology and its effect on the nanoparticles decoration (Fig. S4 and Fig. 3). SEM shows that the samples are formed by small nanocolloids interconnected to each other. This morphology, typical of sol–gel like syntheses, proves that the salt mix melted before

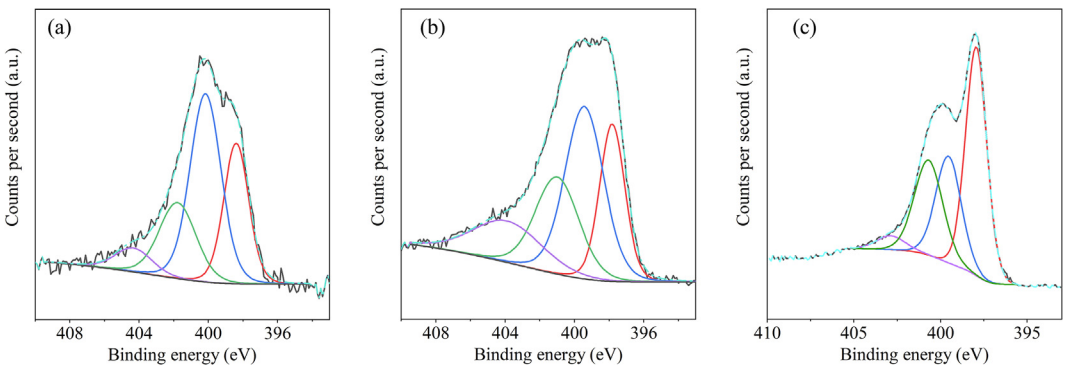

Fig 1. XPS N1 *s* deconvoluted peaks of (a) CLZ, (b) CNZ and (c) CLK. The deconvolution components are represented in different colors: 397 eV (red), 399 eV (blue), 401 eV (green), 403 eV (purple).

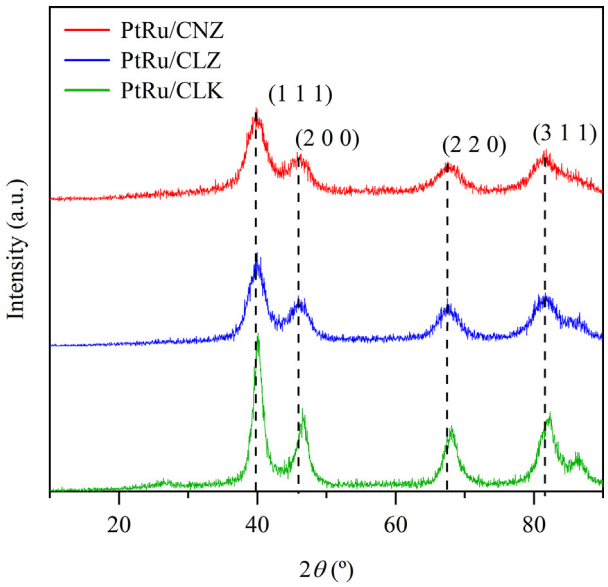

Fig 2. XRD patterns of the different PtRu/NC supported catalysts. Pure Pt fcc diffractions planes are indicated in dashed lines.

the decomposition and condensation of cytosine occurred and were able to solubilize the precursor. Upon increasing the heating treatment temperature, cytosine condensates and colloids start forming similar to what happens in a sol–gel process at much lower temperatures. Despite the same mechanism is valid for all the salt mixes, the different salts foster the formation of colloids of different sizes (i.e., CLZ shows smaller colloids than CNZ and CLK). CLZ TEM micrographs show that the sample has a very rough morphology. The micrographs go along with the observed wide range of mesopore sizes observed for this material. On the other hand, CNZ and CLK present a much smooth surface morphology. Comparison between the fresh supports and PtRu/NCs samples shows how over CLZ and CNZ supports PtRu nanoparticles disperse more homogeneously than over CLK. Nanoparticle size distribution was also measured from TEM micrographs (Fig. S5). The sizes measured by TEM are smaller than those calculated by XRD (Table 1). According to TEM micrographs, PtRu nanoparticles over CLZ, CNZ and CLK are of 2.8 ± 0.6, 3.4 ± 0.8 and 4.3 ± 1.0 nm, respectively. Though, at a first glance, it might seem that larger nitrogen content and lower graphitization degree favor the formation of larger PtRu nanoparticles, the textural properties of the samples must also be taken into consideration. The different between XRD and TEM measurements could be ascribed to the detection limit of XRD (3–4 nm), which prevents from a proper quantification of the final distribution.

Metal oxidation states and the interaction between them and the noble carbon supports were studied through TPR analysis. Fig. 4 displays the profiles for all the synthesized materials. Fresh noble carbon samples only show H_2 consumption peaks at high reduction temperatures (above 400 °C), which are related to the gasification process of the carbonaceous materials. In the case of the PtRu/NC electrocatalysts, all samples present a similar profile with distinct groups of peaks attributed to the presence of oxidized species or interactions between catalyst nanoparticles and support. According to the available literature, the reduction of PtO_x species over carbonaceous supports takes place at temperatures between 100–200 °C [39,40]. In this sense, no significant H_2 consumption is registered for such temperature range, confirming the absence of Pt oxides (in agreement with the XRD essays). The negatives and positives peaks located at low temperatures (50–100 °C) are ascribed to the release of small hydrogen amounts previously adsorbed on the Pt surface [41–43]. Subsequently, all PtRu/NC samples exhibit a broad H_2 consumption peak around to 350 °C associated to the reduction of RuO_2 species [42,44,45]. In addition, areas of such peaks are higher for CNZ and CLZ-based electrocatalyst compared to PtRu/CLK, confirming higher amounts of RuO_2 species in these materials and hence, lower alloying degree.

The textural properties of the samples were analyzed by N_2 and CO_2 adsorption/desorption isotherms at 77 and 273 K (Fig. 5). Table 2 summarizes the main parameters extracted from the isotherms calculated for each of the bared supports and the PtRu decorated samples. CLZ and CNZ show relatively similar specific surface areas (S_{BET} of 1834 and 1701 $m^2\ g^{-1}$, respectively) but differ on the type of isotherm. However, CLZ shows a combination of Type I and Type II isotherms indicative of the presence of both micropores and not-well-defined large mesopores. On the other hand, CNZ shows a Type I and Type IV isotherm which suggests the presence of both micropores and mesopores. The total pore volume ($V_{T,N2}$) of the samples is of 2.06 and 1.04 $cm^3\ g^{-1}$, respectively. Pore size distributions were obtained applying QSDFT method to the adsorption branch of N_2 isotherms. Results show that sample CNZ has indeed a narrow distribution of mesopores of around 2.5 nm. However, sample CLZ is comprised of a wide range of mesopores of different sizes, which are responsible for the larger porous volume observed in the sample (Fig. S6). Similar isotherm shapes were already reported by Antonietti et al. [46], however, the development of such mesoporosity, strongly depends on both the metal mix and the carbonaceous precursor and cannot uniquely be ascribed to the use of LZ. On the other hand, CLK sample shows a much smaller S_{BET} of ca. 65 $m^2\ g^{-1}$ and a V_T of 0.05 $cm^3\ g^{-1}$ according to nitrogen sorption isotherms, which corroborates the importance of the melting temperature of the salts in the formation of a porous network. When loading PtRu nanoparticles, a large decrease in the adsorbed volume of N_2 at low relative pressures correspondent to micropores is observed in the N_2 adsorption–desorption isotherms. Moreover, the significant decrease in the cumulative volume of PSD calculated by QSDFT indicates that also mesopores get block during the metal nanoparticle decoration process. The tortuous nanomorphology of CLZ probably fosters the formation of nucleation seeds while the growth of the nanoparticles is hindered by the mesoporous nature of the sample, which gives rise to smaller nanoparticles. The microporous nature of CNZ also give rise to similar results but the nanoparticles grow slightly larger than over CLZ. Over CLK, the particles seem to collide in small agglomerates probably due to the much lower porous nature of the sample.

CO_2 adsorption and desorption isotherms at 273 K show that CNZ, CLZ and CLK uptake 6, 4.5 and 2 mmol g^{-1}, respectively. The larger uptake of CNZ can be ascribed to its larger content of nitrogen which translates into more electron rich sites that

Table 1
Summary of PtRu/C structural data extracted from XRD patterns and TEM.

Catalyst	Particle size (nm) XRD/TEM	Lattice parameter (nm)	Pt (220) position 2θ (°)	Second metal alloyed (%)
PtRu/CNZ	5.20/3.4 ± 0.8	0.3920	67.56	4.96
PtRu/CLZ	6.21/2.8 ± 0.6	0.3922	67.5	3.31
PtRu/CLK	9.07/4.3 ± 1.0	0.3891	68.1	27.86

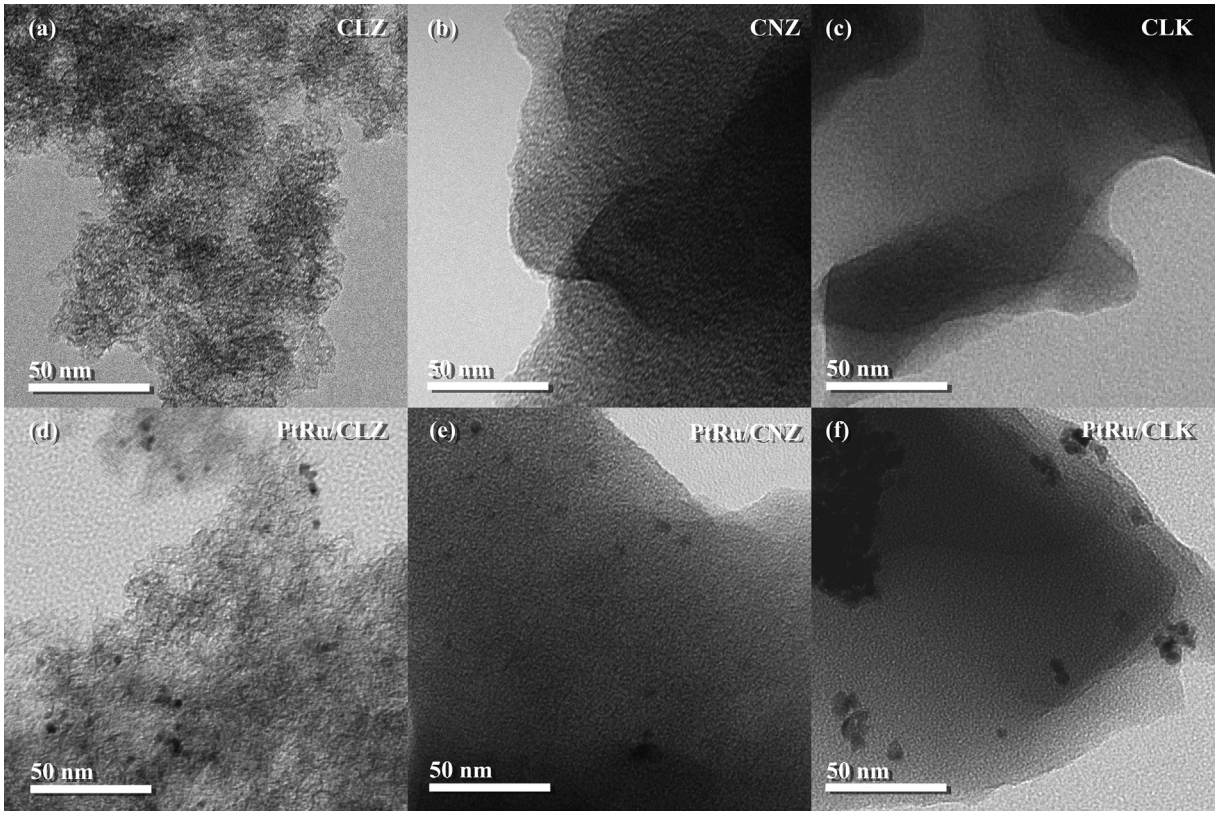

Fig 3. (Top row) TEM micrographs of (a) CLZ, (b) CNZ and (c) CLK. (Bottom row) TEM micrographs of (d) PtRu/CLZ, (e) PtRu/CNZ and (f) PtRu/CLK samples. Scale bare equals 50 nm.

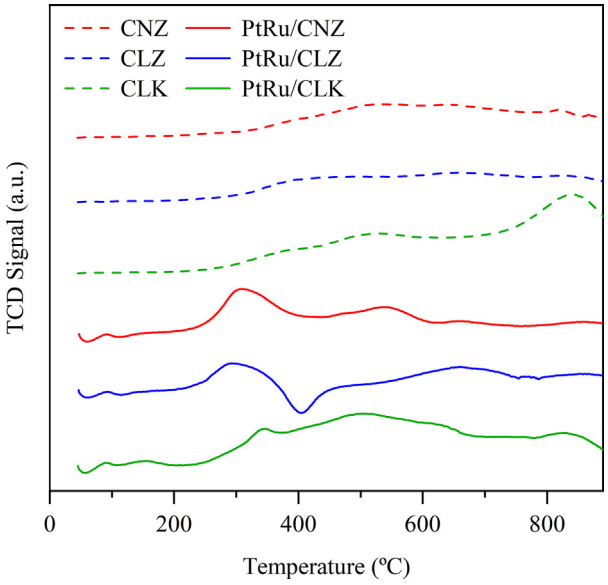

Fig 4. TPR spectra of fresh noble carbon support and PtRu/NC electrocatalysts.

increase the affinity towards CO_2 of the material when compared to CLZ. Of course, a different narrow nanoporous architecture is also plausible. However, the reliability of DFT methods to address this hypothesis was recently questioned in the ultranarrow micropore size, and the differences between the CO_2 pore size distributions of these samples fall precisely in that range [47]. CLK uptake is ascribed to the much less developed porosity of the sample. When loading PtRu nanoparticles, also a decrease of 70% of the total amount of CO_2 adsorbed by the samples was observed indicating that the nanoparticle decoration was able to block also ultra-narrow micropores.

3.2. Electrochemical characterization in a half-cell configuration

The electrochemical properties of PtRu electrocatalysts supported on different noble carbons were evaluated by CV tests. Fig. 6 illustrates the cyclic voltammograms of all synthesized electrodes in 0.25 M $HClO_4$ aqueous solution saturated by N_2 at a scan rate of 50 mV s^{-1} and in a potential range between − 0.068 and 1.36 V vs. RHE. The CV profiles present the typical hydrogen adsorption/desorption peaks (−0.068–0.2 V vs. RHE), the electrochemical double layer region (0.2–0.4 V vs. RHE) and the oxidation/reduction peaks (>0.4 V vs. RHE) [48–51]. The electrooxidation of Pt-H_{ads} to H^+ in the hydrogen adsorption/desorption region (peaks in the forward scan) clearly indicates differences in the Pt nanocrystals associated to a preferential Pt terraces orientation. According to the available literature, until three different well-defined peaks could be registered for pure Pt at low potential values [52,53]. However, in this study only one peak is identified for all PtRu/NC electrocatalysts (close to 0.01 V vs. RHE), ascribed to a preferential orientation of Pt (1 1 0) and (1 1 1)-types in a lesser extent. This is characteristic of the Ru addition, which could modify the crystalline structure of Pt leading to an only broad and less defined adsorption hydrogen peak as typically reported [54–56]. In addition, note that the intensity of these peaks experiments a considerably drop (PtRu/CLZ > PtRu/CNZ > PtRu/CLK) with the rise of the alloying degree between Pt and Ru species (3.3%, 5% and 27.8% for PtRu/CLZ, PtRu/CNZ and PtRu/CLK, respectively). This can be accounted for the segmental substitution of the Pt surface sites with Ru atoms which causes a loss in the Pt orien-

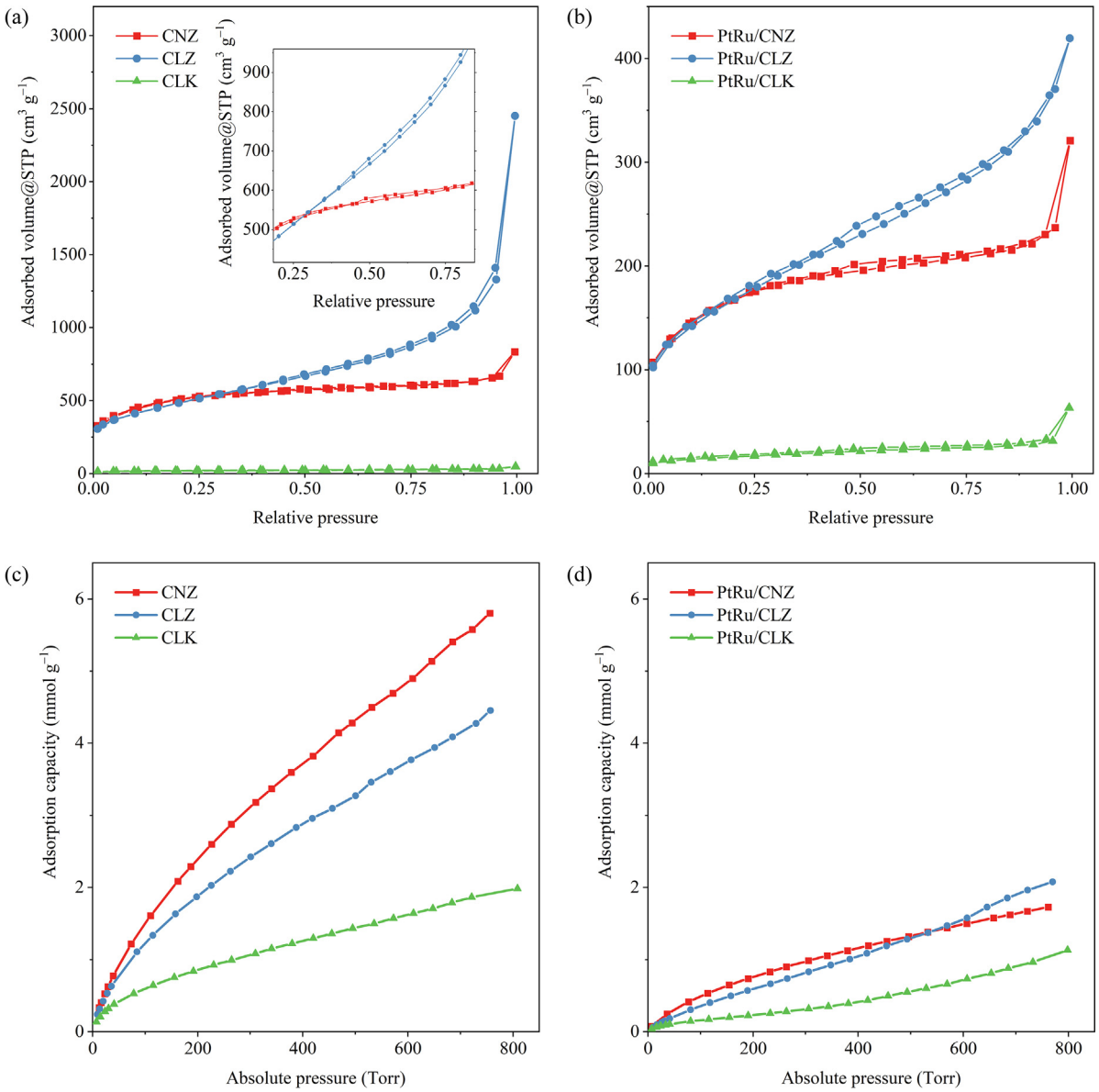

Fig 5. (a) N_2 sorption isotherms at 77 K and hysteresis zoom in inset. (b) CO_2 sorption isotherms at 273 K of CLZ, CNZ and CLK. (c) N_2 sorption isotherms at 77 K and (d) CO_2 sorption isotherms at 273 K of PtRu/CLZ, PtRu/CNZ and PtRu/CLK.

Table 2
Textural parameters calculated for carbonaceous materials and PtRu decorated samples from N_2 and CO_2 physisorption isotherms at 77 and 273 K, respectively.

Catalyst	S_{BET} ($m^2\ g^{-1}$) [a]	$V_{T,N2}$ ($cm^3\ g^{-1}$) [b]	$V_{mic,CO2}$ ($cm^3\ g^{-1}$) [c]
CNZ	1701	1.04	0.23
CLZ	1834	2.06	0.18
CLK	65	0.05	0.08
PtRu/CLZ	593	0.37	0.08
PtRu/CNZ	594	0.37	0.07
PtRu/CLK	57	0.05	0.13

[a] Specific surface area was calculated from nitrogen adsorption data (P/P_0 < 0.2) using the BET method. [b] Total pore volume (V_T) was calculated from the amount of nitrogen adsorbed at P/P_0 = 0.995. [c] Total micropore volume was calculated from the amount of carbon dioxide adsorbed at 730 Torr.

tated monocrystals and consequently, a drop in the Pt (1 1 0) and (1 1 1)-types sites [57,58]. Generally, all synthesized anodes present similar features in both, the double layer and the oxidation/reduction regions which are indicative of the hydrophilic behavior of the catalyst and the possible oxides formation. In this context, Ru presence promotes the formation of oxygen-containing species adsorbed on the catalyst surface which may boost the alcohol oxidation reaction [59–62]. The ECSA of PtRu/NC electrocatalysts was calculated by integrating the hydrogen adsorption/desorption areas of the cyclic voltammograms [51,63,64]. All values are listed in Table 3. The highest ECSA value was obtained for PtRu/CLZ, followed by PtRu/CNZ and PtRu/CLK (i.e., following the same trend as the data obtained by physisorption analysis), indicating that more electrochemically active sites are available on the PtRu nanoparticles supported on CLZ noble carbon, due to the low alteration of the Pt nanocrystal structure. Therefore, the fraction of Pt available to participate in the electrode reactions is lower while the alloy degree increases. On the other hand, the stability and the degradation rate of the synthesized electrocatalyst were explored through an accelerated degradation test (ADT). To that purpose, CV essays were conducted at the same conditions for 500 cycles in order to evaluate the ECSA variation. Normally, a progressive loss in the ECSA, while increasing the cycling process, is usually reported

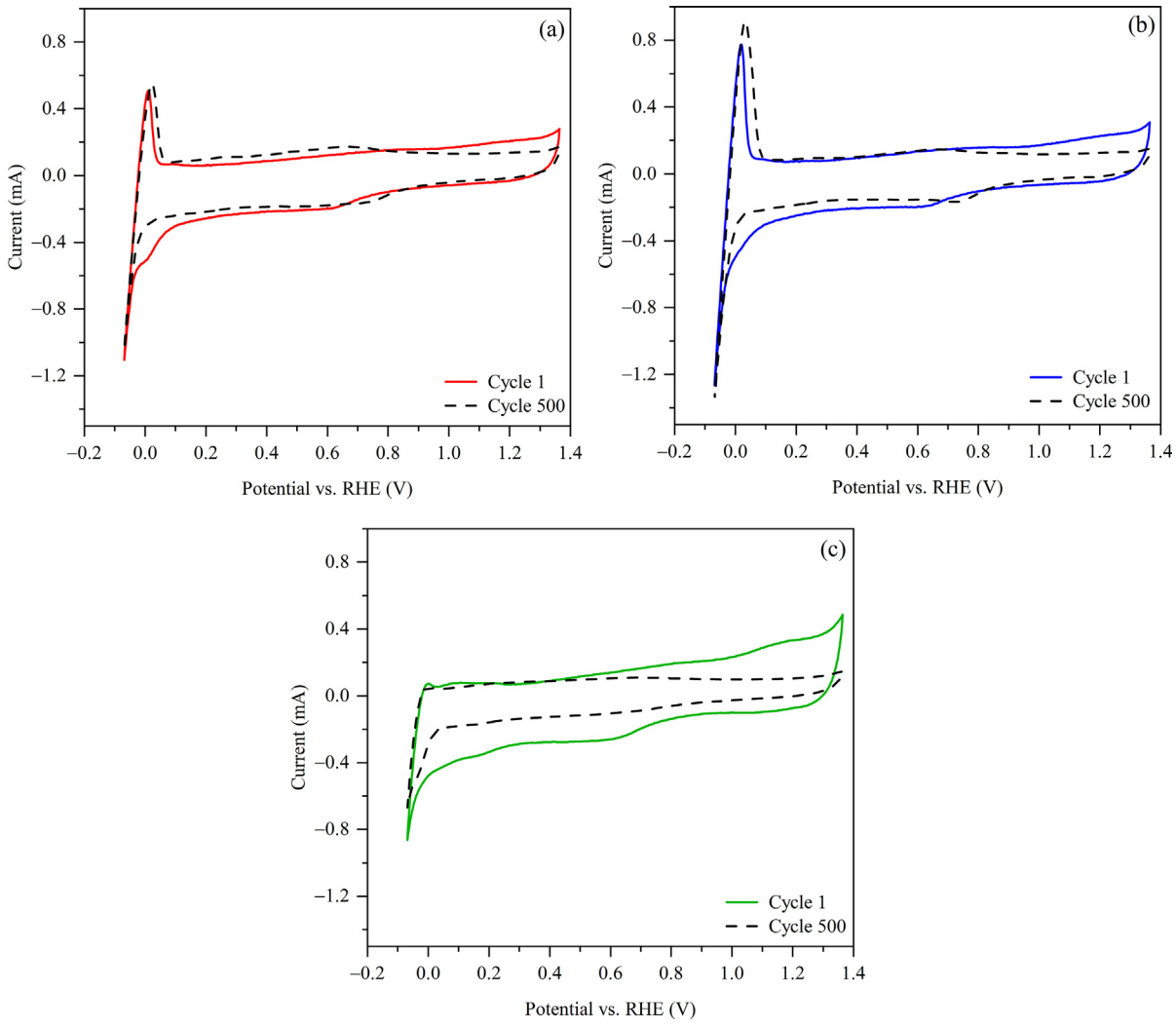

Fig 6. CV curves of the electrocatalysts in N_2-purged 0.5 M $HClO_4$, at room temperature and 50 mV s^{-1} of scan rate. (a) PtRu/CNZ, (b) PtRu/CLZ and (c) PtRu/CLK.

Table 3
ECSA values for the different PtRu/NC catalysts calculated from adsorption/desorption hydrogen peaks.

Catalyst	ECSA (m^2 g^{-1})		Degradation (%)
	Cycle 1	Cycle 500	
PtRu/CNZ	18.37	14.96	18.58
PtRu/CLZ	23.94	26.05	−8.81
PtRu/CLK	16.73	11.54	31

due to the Pt and Ru dissolution-redeposition process with the consequent metallic species migration through the catalyst surface. This phenomenon is known as the Ostwald ripening effect and implies an agglomeration of the catalyst nanoparticles [65]. In case of PtRu/NC, low degradation degrees are registered for CNZ and CLK-based electrocatalyst (i.e. 15%–30%, Table 3). PtRu/CLZ exhibits a slight increase in the ECSA after the ADT (from 24 to 26 m^2 g^{-1}), which could be attributed to a cleaning process of the catalyst surface, leading to a small activation of the electrocatalyst. Although it has been proved that the sintering effect takes place in a lesser extent for alloyed catalysts [66], PtRu/CLK presents the highest ECSA losses compared with the rest of NC-based electrocatalysts associated to a lower alloying degree. In this sense, the interaction between the active metals and support would play an essential role in the degradation process. Accordingly, it seems that PtRu nanoparticles remains strongly fixed to CNZ and CLZ-based supports, while such interactions are weaker when CLK-derived materials are used. This could be also related to PtRu nanoparticles dispersion and hence to the particle size. Thus, electrocatalysts with smaller particle sizes prove to be more resistant to the metal dissolution-redeposition process. However, it is important to highlight that, in general terms, all degradation degrees are quite low compared to those obtained for similar active metal phases supported on other materials such as Vulcan XC-72 (40%–60% of degradation after the ADT) [20,66]. This can be accounted for the high surface areas offered by the noble carbon-based materials preventing the particles sintering.

In order to go one step further, the electrochemical activity of the synthesized PtRu/NC catalysts has been investigated in a N_2-saturated 4 M ethanol solution with different $HClO_4$ concentrations. Fig. 7 displays the CV tests at a scan rate of 10 mV s^{-1} and a potential range between – 0.2–1.2 V vs. RHE. The apparition of two distinct peaks can be observed during the forward and reverse scans which are related to a particular step of the EOR. It is well known that the EOR follows a complex reaction mechanism involving numerous multi-step reaction pathways that lead the production toward several groups of by-products. Many authors have studied the ethanol oxidation mechanism on monometallic Pt/C through different electrochemical and *in-situ* characterization

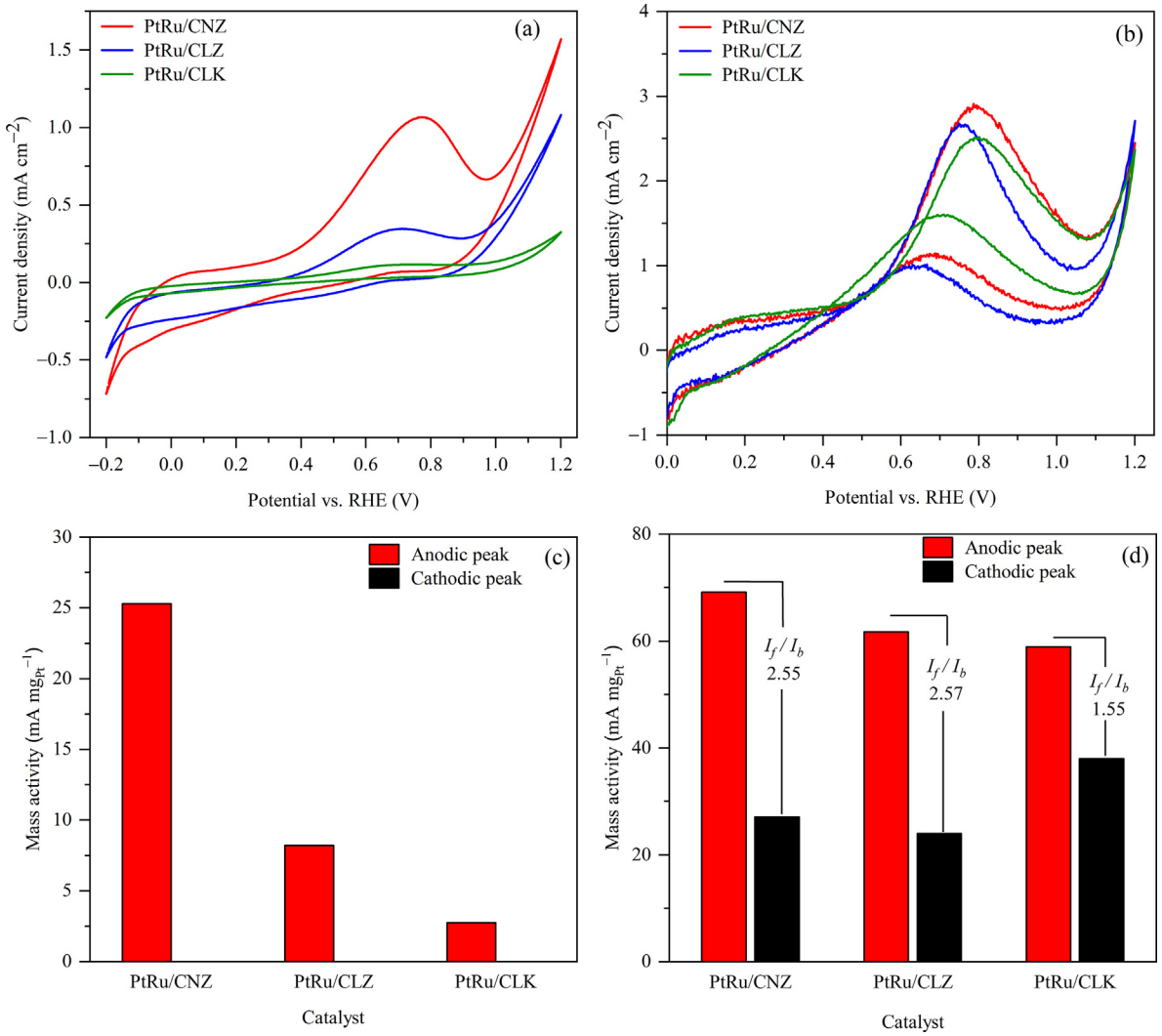

Fig 7. EOR performance of the synthesized PtRu/NC electrocatalysts in 4 M Ethanol solution with different $HClO_4$ concentrations at room temperature and 10 mV/s of scan rate. (i) CV tests at 0.004 M $HClO_4$ (a) and 0.5 M $HClO_4$ (b). (ii) Mass activity and I_f/I_b ratio for 0.004 M $HClO_4$ (c) and 0.5 M $HClO_4$ (d) concentrations.

techniques [67–69]. In case of bimetallic Pt-Ru catalysts, a generally accepted pathway includes the following steps:

$$Pt^* + CH_3 - CH_2OH \rightleftarrows Pt - CHOH - CH_3 + H^+ + e^-, \quad (1)$$

$$Pt - CHOH - CH_3 \rightleftarrows CHO - CH_3 + H^+ + e^- + Pt^*, \quad (2)$$

$$Pt^* + CHO - CH_3 \rightleftarrows Pt - CO - CH_3 + H^+ + e^-, \quad (3)$$

$$Ru^* + H_2O \rightleftarrows Ru - OH + H^+ + e^-, \quad (4)$$

$$Pt - CO - CH_3 + Ru - OH \rightleftarrows COOH - CH_3 + Pt^* + Ru^*, \quad (5)$$

$$Pt - CO - CH_3 + Pt \rightleftarrows Pt - CO + Pt - CH_3. \quad (6)$$

In this context, ethanol electrooxidation process takes place through a bi-functional mechanism boosted by the bimetallic PtRu catalyst. Adsorption and ethanol dissociation mainly occur in the Pt active sites with the consequent intermediate species generation, adsorbed on the catalyst surface (Equations 1–3). Conversely, oxidant species formation (OH_{ads}) requires water dissociation that takes place more efficiency (lower potentials) on Ru surface, increasing the number of transferred electrons (Equations 4 and 5). Based on the above, peaks registered in the forward direction can be attributed to the oxidation of freshly chemisorbed species [70,71], while reverse ones correspond to the re-oxidation of ethanol and intermediate species that are formed from the incomplete oxidation in the forward scan [72–74]. On the other hand, at high potentials values, oxide species from water dissociation cover the electrocatalyst surface which leads to a decrease in the current density. The reduction of such oxides species during the backward scan allows the ethanol re-oxidation due to the re-activation of the catalyst surface. Fig. 7(a) shows the EOR performance for the different PtRu/NC electrocatalysts at low perchloric acid concentrations (0.004 M). PtRu/CNZ exhibits the greatest current density value in the forward scan (1.06 mA cm^{-2}), which is 3 and 9 times higher than that of PtRu/CLZ (0.34 mA cm^{-2}) and PtRu/CLK (0.11 mA cm^{-2}), respectively. Therefore, differences in the catalytic performance reveal a marked effect of noble carbon support toward the EOR process. In addition, the oxidation peaks in the reverse scan are difficult to identify (at these electrolyte conditions) probably due to the low advance in the oxidation process. At higher perchloric acid concentrations (0.5 M, Fig. 7b), the current density values experiment a huge increase due to an enhancement of the anodic charge transfer reaction kinetics and the ionic conductivity of the anolyte solution by decreasing the pH [1,75]. Note that, in this case, all pro-

files show a reverse oxidation peak from 0.7 V vs. RHE. This can be attributed to the rise in the reaction kinetics that implies a deeper progress in the EOR process. Although the variation in the electrochemical performance obtained for the different materials is lesser at higher $HClO_4$ concentrations, the general trend remains the same, achieving the highest activity for PtRu/CNZ followed by PtRu/CLZ and PtRu/CLK. Taking into account that the metal active phase is the same for all the synthesized materials, such behavior in the EOR performance could be explained in terms of the following aspects: (i) Pt particle sizes of CNZ and CLZ-based electrocatalyst are smaller compared to PtRu/CLK which results in a better metals dispersion and metal-support interaction, preventing the sintering effect of the catalyst (less degradation degree). Furthermore, the conversion rate tends to increase for smaller particles sizes. (ii) The alloying degree between Pt and Ru is another parameter to consider (up to 28% for PtRu/CLK and between 3%–5% for PtRu/CLZ and PtRu/CNZ). Generally, alloyed nanoparticles promote the alcohol electrooxidation at low potentials levels, enhancing the kinetics [6]. However, high percentages could dramatically decrease the Pt fraction available for the suitable development of the electrochemical reaction (as reflected in the ECSA results), hindering the ethanol adsorption and dissociation process (Equations 1 and 2). (iii) Finally, the elemental composition of the NC support could be postulated as a key aspect influencing the electrochemical performance. In this sense, it seems that materials with higher N-containing groups (CNZ > CLZ) and hence, more electron rich sites (confirmed through CO_2 isotherms essays) could promote the electrochemical reaction. In addition, other authors have reported that the position of such N-species (in particular quaternary/graphitic-N) plays an important role in the electrochemical reactions, enhancing the electron transfer [76,77]. On the other hand, to evaluate the resistance upon oxidation of the proposed carbonaceous materials during the EOR, CVs essays were conducted for the different NC supports in the reaction environment at a higher potential interval (0–1.8 V vs. RHE). As can be seen in Fig. S7, no significant current density contributions are noticeable for these materials in comparison with the glassy carbon tip profile (blank), which indicates a suitable stability of the NCs upon oxidation.

Fig. 7(c–d) shows the EOR activity normalized to the Pt loading (mass activity) for both, direct (I_f) and reverse (I_b) peaks at the different $HClO_4$ concentrations. Although the I_f/I_b ratio has been commonly used as indicator of the carbon intermediates tolerance [78–80], previous studies have proved that this parameter is more related to the oxidation/reduction dynamics of the electrocatalyst surface rather than the poison ability [81,82]. In this context, a high I_f/I_b ratio implies less re-activation of the electrocatalyst surface during the backward scan (low I_b peak) due to the presence of larger amounts of oxide species. As oxophilicity is the tendency of a chemical compound to form surface oxygenated species, the higher the I_f/I_b ratio, the higher the degree of oxophilicity of the electrocatalyst, or in other words, the ability to dissociate water. Accordingly, CNZ and CLZ-based electrocatalyst exhibit better I_f/I_b ratios (2.5) compared to that obtained for PtRu/CLK (1.5), promoting the OH^- species formation. This enhancement could be ascribed to the strong interplay between PtRu nanoparticles and the noble carbon support which could result in a more efficient removal of the carbonaceous intermediates on the electrocatalysts active sites. Table 4 [2,5–12,83,84] compares the main electrochemical properties of similar Pt-based catalyst supported on different materials with those presented in the current work. In general terms, promising mass activity and I_f/I_b values are achieved by PtRu/CNZ (69.1 mA mg^{-1} and 2.5, respectively), which demonstrates the efficiency of NC-type supports toward the EOR. To evaluate the CO-tolerance, CO-stripping essays were conducted for the different PtRu/NCs samples. Fig. S8 depicts the obtained profiles in a 0.5 M $HClO_4$ solution at 20 mV s^{-1} of scan rate and a potential range between 0–1.2 V vs. RHE. Prior to each test, the electrolyte was saturated with a CO stream. The CVs in N_2 saturation conditions are also shown for comparison purposes. CO-stripping curves show that the CO_{ads} oxidation takes place at a more negative potential on PtRu/CNZ (0.88 V vs. RHE) compared to CLZ and CLK-based electrocatalyst (0.91 and 0.96 V, respectively), which indicates the substantially enhanced CO tolerance of PtRu/CNZ. This is in good agreement with the previous CVs test where this electrocatalyst exhibited the best electrochemical performance. Note that although the intermediate removal is more favored on PtRu/CNZ surface, the peak area for the CO oxidation is slightly higher for PtRu/CLZ. This may be due to the increased availability of the Pt active sites shown by this electrocatalyst, as previously determined in the ECSA calculation. Finally, the stability of the PtRu/NCs was explored through long-term galvanostatic tests. Fig. S9 depicts the potential vs. time profile for each synthesized material in a 4 M ethanol + 0.5 M $HClO_4$ M solution at a fixed current density of 1 mA cm^{-2} for 10 h. An initial increase of the potential is observed during the first minutes of operation which is accounted for an initial adsorption of intermediate species (derived from the ethanol partial oxidation), increasing the coverage degree of the electrocatalyst surface. From this point on, the system seems to attain a steady state leading to a stable potential value. In general terms, PtRu/CNZ provides a superior electrocatalytic activity, followed by PtRu/CLZ and PtRu/CLK being in consonance with the previous results. Also, similar shapes can be observed in the glassy carbon tip images before and after the chrono test, which proves that there is no detachment of the catalytic layer as a consequence of metals dissolution (Fig. S10).

All electrochemical parameters considered, CNZ and CLZ-based electrocatalysts were selected as the best anodes for the subsequent scale-up of the system to a PEM cell in order to develop the EOR process for real devices (ethanol electrochemical reforming).

3.3. Electrocatalytic experiments in a full PEM cell

LSV essays have been carried out in a potential range from 0 to 1.4 V, at a scan rate of 20 mV s^{-1} and at a constant temperature of 80 °C. Fig. 8(a) depicts the electrochemical performance of the different PtRu/NC in a 4 M ethanol solution. Once again, PtRu/CNZ exhibits the highest current density values (262 mA cm^{-2}) and hence, the best electrocatalytic activity, being in consonance with the behavior obtained in the half-cell experiments. A slight decrease in the polarization curve slope can be observed at high potential values, which could be assigned to small mass transfer limitations. Furthermore, both the onset potential (0.3–0.4 V) and the current density reached (220–262 mA cm^{-2}) are similar to those obtained for other ethanol electroreforming studies at similar conditions [1,2,75].

In order to evaluate the behavior of the system at real operating conditions (i.e., static tests), chronopotentiometry essays have been also conducted in a 4 M ethanol/water solution at 80 °C and for different applied current steps (i.e. 0.2, 0.4, and 0.6 A which corresponds to 40, 80 and 120 mA cm^{-2}, respectively) for 15 min. Fig. 8(b) shows the cell potential variation vs. time on stream for each synthesized electrocatalyst in the whole applied current range of study. As expected, an increase in the applied current leads to a rise in the cell potential and hence, a higher cell energy consumption. Although PtRu/CNZ showed a superior electrochemical performance in the previous essays (CVs and LSVs), in this case both anodes exhibit a similar profile, being CNZ-based electrocatalyst slightly more efficient at high applied current levels (lower cell potential at 0.6 A). Generally, cell potential remains stable in the intermediate applied current region (0.2–0.4 A), mainly for the lowest galvanostatic level, which is indicative of the stability of

Table 4
Overview of electrochemical properties of Pt-based electrocatalysts on different supports.

Catalyst	Conditions	Onset potential (V)	Mass activity (mA mg^{-1})	I_f/I_b	Reference
PtRu/CNZ	4 M EtOH + 0.5 M $HClO_4$	0.4 vs. RHE	69.1	2.55	This work
Pt/CCE	0.15 M EtOH + 0.2 M H_2SO_4	0.2 vs. SCE	22.5	1.13	[11]
PtRu/ZrO_2-Rh	0.5 M EtOH + 0.2 M H_2SO_4	0.3 vs. RHE	64.0	1.88	[83]
PtRu/C	1 M EtOH + 1 M KOH	−0.5 vs. Hg/HgO	74	1.66	[6]
PtRu/WO_3-ZrO_3	0.5 M EtOH + 0.5 M H_2SO_4	0.32 vs. RHE	27.5	2.20	[84]
PtRu/A-FWCNT	1 M EtOH + 0.1 M NaOH	0.2 vs. RHE	3.0	–	[12]
PtRu/CNF600	2 M EtOH + 0.5 M H_2SO_4	0.3 vs. RHE	70.0	1.17	[9]
PtRu/TECNF	2 M EtOH + 0.5 M H_2SO_4	0.4 vs. RHE	250.0	0.83	[9]
PtRu/TiO_2	2 M EtOH + 0.5 M H_2SO_4	0.4 vs. RHE	18.0	0.72	[10]
PtRuSn/C	0.5 M EtOH + 0.5 M H_2SO_4	0.3 vs. RHE	45.0	1.29	[5]
PtSn/C	0.5 M EtOH + 0.1 M KOH	0.45 vs. RHE	112.9	1.20	[7]
PtSn/CNFLS	0.5 M EtOH + 0.5 M H_2SO_4 / 80 °C	0.45 vs. RHE	31.0	–	[2]
Pt(Cu)/C	0.17 M EtOH + 0.5 M H_2SO_4	0.3 vs. RHE	16.9	2.33	[8]

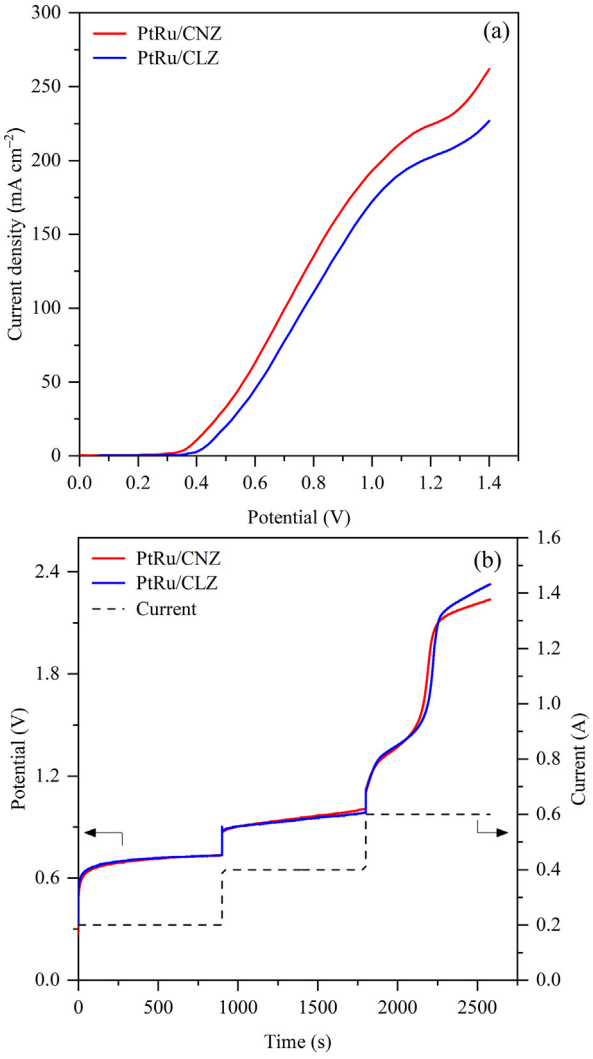

Fig 8. Electroreforming essays in a PEM electrolysis cell at 80 °C in a 4 M ethanol solution. (a) LSV tests at 20 mV s^{-1} of scan rate between 0–1.4 V. (b) Chronopotentiometry measurements at different applied current levels (0.2–0.6 A).

the system. In contrast, for higher demanded currents (0.6 A) both anodes experiment an exponential increase in the required potential, stabilizing at values above 2 V. Considering that theoretical onset potential for water electrolysis is close to 1.23 V, the potential range required for this current applied level could lead to the simultaneous electrooxidation of both molecules (ethanol and water). To assess the total ethanol conversion and the product distribution (H_2 and organic compounds), the reaction products derived from the ethanol electrochemical process have been analyzed at each galvanostatic step. Main results are summarized in Table 5. As expected, similar hydrogen flow rates are registered for both electrocatalysts since such production is dictated by the applied current (Faraday's law). In addition, Fig. S11 displays the comparison between the experimental hydrogen measurements and the theoretical ones, for the different as-prepared PtRu/NC electrocatalysts in the interval of study. Note that experimental data are quite similar to those calculated via Faraday's law in all cases, confirming the absence of faradaic losses. Regarding organic compounds production, only acetaldehyde (AAL) and ethyl acetate (EA) are registered for all the galvanostatic steps. This is not a surprise, since under the current operating conditions the acetaldehyde pathway is favored versus the production of other (more oxidized) compounds such as CO_2, which are promoted at lower initial ethanol concentrations and cell potentials (<0.1 M and < 0.5 V) [85,86]. Taking into account all production flow rates, it is possible to evaluate the closing balance for the overall electrochemical process (Fig. S12) by comparing the experimental hydrogen value with the stoichiometric one (equivalent H_2 calculated from the experimental organic compounds measurements). In other words, verifying that the organic compounds generation and the hydrogen production follow a suitable stoichiometric correlation. Thus, similar AAL and EA production rates are obtained for both anodes at intermediates applied current levels achieving analogous ethanol conversion values per cell pass (close to 1.2% and 2.5% at 0.2 and 0.4 A, respectively). Also, the products balance properly fits showing no significant difference between experimental and stoichiometric values (error < 5%). In contrast, it can be observed that at the highest galvanostatic step (0.6 A), the organic compounds production slightly increases for PtRu/CNZ, which is not consistent with the rise of the hydrogen flow rate. Even a considerably decrease in the AAL and EA flow rates is registered for PtRu/CLZ at this applied current level, leading to a marked difference between the experimental and stoichiometric hydrogen in the closing balance adjustment (Fig. S12). This can be ascribed to the oxygen evolution reaction (OER), which takes place simultaneously with the EOR, confirming that part of the hydrogen amount proceeds via water electrolysis (around 28% and 61% of the total production for PtRu/CNZ and PtRu/CLZ, respectively). In this sense, CNZ-based anode achieved a higher ethanol conversion rate (2.9%) and hence, better efficiency in the ethanol electroreforming process compared to the CLZ-based one (1.5%). However, it should be highlighted that the operation at such high potential values (>1.4 V) would be unattractive from the alcohol oxidation perspective, being more advantageous to operate in the isolate EOR region (0.6–1.2 V). Also, at very high polarization levels, both metal active

Table 5
Product distribution of the PtRu/NC electrocatalysts obtained from the chronopotentiometry tests.

	Current (A)	H_2(mol min^{-1})	H_2 Percentage (%)		AAL(mol min^{-1})	EA(mol min^{-1})	EtOH conversion(%)
			From EtOH	From H_2O			
PtRu/CNZ	0.2	5.91E − 05	100	–	5.82E − 05	–	1.21
	0.4	1.22E − 04	100	-	1.15E − 04	2.96E − 06	2.52
	0.6	1.87E − 04	72	28	1.32E − 04	2.77E − 06	2.87
PtRu/CLZ	0.2	5.97E − 05	100	–	5.97E − 05	–	1.24
	0.4	1.21E − 04	100	-	1.24E − 04	2.60E − 06	2.7
	0.6	1.86E − 04	39	61	7.07E − 05	1.45E − 06	1.53

phase and carbons support are more susceptible to be oxidized which could hinder the efficiency of the system.

Finally, from the potential vs. time profile it is possible to calculate the total energy requirements, expressed in kWh per kg of H_2 produced. Main results at each galvanostatic steps are listed in Table S3. In general terms, low energy consumption values (18–25 kWh kgH_2^{-1}) are obtained for both anodes in the intermediate applied current range (0.2–0.4 A), being similar to those obtained in other studies [2,87]. For the highest demanded current (0.6 A), consumption values increase considerably with the potential rise, which implies the EOR limit leading to the simultaneous water–ethanol electrooxidation. Despite this, it is important to mention that all energy requirements are quite low in comparison with that commonly reported for a water electrolysis stack (50 kWh kgH_2^{-1}) [87].

All in all, this work provides an innovation in the electrocatalyst development for EOR, and although further optimization could be carried out, it opens the field of study into the use of new carbonaceous materials for electrochemical applications.

4. Conclusions

In this study different noble carbon materials derived from cytosine were proposed as anode supports for ethanol electrolysis. LiCl/$ZnCl_2$, NaCl/$ZnCl_2$ and LiCl/KCl salt mixtures were used as structure directing agents for cytosine, while PtRu/NC electrocatalysts were synthesized through the modified polyol method. Morphology of the NC materials (porosity, basicity and elemental composition) was found to markedly affect the EOR performance. CNZ and CLZ presented huge specific surface areas (around 1800 $m^2\ g^{-1}$), while CLK reached lower values (around 65 $m^2\ g^{-1}$) due to the salt precursors behavior during the melting process. Resulting differences in the porosity of the samples influenced PtRu particle size distribution and alloy formation, obtaining smaller nanoparticles (3 nm), a lower PtRu alloy degree and higher ECSA values for PtRu/CNZ and PtRu/CLZ. Although all electrocatalysts exhibited high stability during the ADTs, the highest electrocatalytic activity was achieved by using PtRu/CNZ, followed by PtRu/CLZ attributed to the better nanoparticles dispersion and the elemental composition of the carbonaceous support. In contrast, CLK-based electrocatalyst showed lower electrochemical performance due to its reduced mesoporous network and the excess of alloy formation, decreasing the availability of Pt active sites. Finally, the electrochemical reforming process was proved to be feasible at low energy requirements (18–25 kWh kgH_2^{-1}) in a PEM electrolyzer configuration on PtRu/CNZ, leading to a faradaic H_2 production up to 4.5 mL min^{-1} STP in combination with acetaldehyde, as the major intermediate product, and ethyl acetate.

Declaration of Competing Interest

The authors declare that they have no known competing financial interests or personal relationships that could have appeared to influence the work reported in this paper.

Acknowledgments

We gratefully acknowledge the Spanish Ministry of Science and Innovation (State Research Agency. Project PID2019-107499RB-100) for the financial support. The Max Planck Society is also gratefully acknowledged for financial support. J. Brandt is gratefully acknowledged for the help provided during ICP analyses. A. Voelkel is gratefully acknowledged for the help provided with TGA and ECA analyses. H. Runge is gratefully acknowledged for the help provided with electron microscopy images.

Appendix A. Supplementary data

Supplementary data to this article can be found online at https://doi.org/10.1016/j.jechem.2021.07.004.

References

[1] A.B. Calcerrada, A.R. de la Osa, J. Llanos, F. Dorado, A. de Lucas-Consuegra, Appl. Catal. B: Environ. 231 (2018) 310–316.
[2] A.B. Calcerrada, A.R. de la Osa, E. Lopez-Fernandez, F. Dorado, A. de Lucas-Consuegra, Int. J. Hydrogen Energy 44 (2019) 10616–10626.
[3] M.A.F. Akhairi, S.K. Kamarudin, Int. J. Hydrogen Energy 41 (2016) 4214–4228.
[4] E. Antolini, J. Power Sources 170 (2007) 1–12.
[5] G. Wu, R. Swaidan, G. Cui, J. Power Sources 172 (2007) 180–188.
[6] J.C.M. Silva, S. Ntais, V. Rajaraman, É. Teixeira-Neto, Â.A. Teixeira-Neto, A.O. Neto, R.M. Antoniassi, E.V. Spinacé, E.A. Baranova, Electrocatalysis 10 (2019) 203–213.
[7] J. Torrero, M.A. Peña, M. Retuerto, L. Pascual, S. Rojas, Electrochim. Acta 319 (2019) 312–322.
[8] M. Ammam, E.B. Easton, J. Power Sources 222 (2013) 79–87.
[9] D. Sebastián, I. Suelves, E. Pastor, R. Moliner, M.J. Lázaro, Appl. Catal. B: Environ. 132–133 (2013) 13–21.
[10] N. Nakagawa, Y. Ito, T. Tsujiguchi, H. Ishitobi, J. Power Sources 248 (2014) 330–336.
[11] H. Razmi, E. Habibi, H. Heidari, Electrochim. Acta 53 (2008) 8178–8185.
[12] P. Kanninen, M. Borghei, J. Hakanpää, E.I. Kauppinen, V. Ruiz, T. Kallio, J. Electroanal. Chem. 793 (2017) 48–57.
[13] M. Antonietti, M. Oschatz, Adv. Mater. 30 (2018) 1–10.
[14] CN103880758A - Synthesis method of cytosine - Google Patents.
[15] J. Kossmann, D. Piankova, N.V. Tarakina, J. Heske, T.D. Kühne, J. Schmidt, M. Antonietti, N. López-Salas, Carbon 172 (2021) 497–505.
[16] J. Kossmann, T. Heil, M. Antonietti, N. López-Salas, ChemSusChem 13 (2020) 6643–6650.
[17] T.W. van Deelen, C. Hernández Mejía, K.P. de Jong, Nat. Catal. 2 (2019) 955–970.
[18] S. Jayabal, G. Saranya, D. Geng, L.-Y. Lin, X. Meng, J. Mater. Chem. A 8 (2020) 9420–9446.
[19] E.A. Baranova, C. Bock, D. Ilin, D. Wang, B. MacDougall, Surf. Sci. 600 (2006) 3502–3511.
[20] A. Rodríguez-Gómez, F. Dorado, A. de Lucas-Consuegra, A.R. de la Osa, J. Energy Chem. 56 (2021) 264–275.
[21] A. Rodríguez-Gómez, F. Dorado, A. de Lucas-Consuegra, A.R. de la Osa, Chem. Eng. J. 402 (2020) 125298.
[22] M.D. Oza, R. Meena, A.K. Siddhanta, Carbohydr. Polym. 87 (2012) 1971–1979.
[23] S. Zhang, K. Dokko, M. Watanabe, Mater. Horiz. 2 (2015) 168–197.
[24] N. Fechler, T.-P. Fellinger, M. Antonietti, Adv. Mater. 25 (2013) 75–79.
[25] L. Liu, S.J. Tan, T. Horikawa, D.D. Do, D. Nicholson, J. Liu, Adv. Colloid Interface Sci. 250 (2017) 64–78.
[26] Y. Wang, X. Zhang, A. Li, M. Li, Chem Commun. 51 (2015) 14801–14804.
[27] T.S. Miller, A.B. Jorge, T.M. Suter, A. Sella, F. Corà, P.F. McMillan, Phys. Chem. Chem. Phys. 19 (24) (2017) 15613–15638.
[28] P. Kuhn, M. Antonietti, A. Thomas, Angew. Chem. Int. Ed. 47 (2008) 3450–3453.
[29] A. Dutta, J. Ouyang, ACS Catalysis 5 (2015) 1371–1380.

[30] N. Erini, R. Loukrakpam, V. Petkov, E.A. Baranova, R. Yang, D. Teschner, Y. Huang, S.R. Brankovic, P. Strasser, ACS Catalysis 4 (2014) 1859–1867.
[31] J. Sulaiman, S. Zhu, Z. Xing, Q. Chang, M. Shao, ACS Catalysis 7 (2017) 5134–5141.
[32] X. Qin, L. Zhang, G.-L. Xu, S. Zhu, Q. Wang, M. Gu, X. Zhang, C. Sun, P.B. Balbuena, K. Amine, M. Shao, ACS Catalysis 9 (2019) 9614–9621.
[33] R. Chetty, W. Xia, S. Kundu, M. Bron, T. Reinecke, W. Schuhmann, M. Muhler, Langmuir 25 (2009) 3853–3860.
[34] C. Bock, C. Paquet, M. Couillard, G.A. Botton, B.R. MacDougall, J. Am. Chem. Soc. 126 (2004) 8028–8037.
[35] H. Yang, C. Coutanceau, J.M. Léger, N. Alonso-Vante, C. Lamy, J. Electroanal. Chem. 576 (2005) 305–313.
[36] J. Solla-Gullón, F.J. Vidal-Iglesias, J.M. Feliu, Annu. Rep. Prog. Chem. C 107 (2011) 263–297.
[37] E. Antolini, F. Colmati, E.R. Gonzalez, Electrochem. Commun. 9 (2007) 398–404.
[38] G.A. Jeffery, J. Chem. Educ. 34 (1957) A178.
[39] Y.C. Wei, C.W. Liu, W.J. Chang, K.W. Wang, J. Alloys Compd. 509 (2011) 535–541.
[40] S.Y. Huang, S.M. Chang, C.T. Yeh, J. Phys. Chem. B 110 (2006) 234-239.
[41] I. Gandarias, P.L. Arias, J. Requies, M.B. Güemez, J.L.G. Fierro, Appl. Catal. B: Environ. 97 (2010) 248–256.
[42] H. Yan, S. Yao, B. Yin, W. Liang, X. Jin, X. Feng, Y. Liu, X. Chen, C. Yang, Appl. Catal. B: Environ. 259 (2019).
[43] J. Guo, G. Sun, S. Shiguo, Y. Shiyou, Y. Weiqian, Q. Jing, Y. Yushan, X. Qin, J. Power Sources 168 (2007) 299–306.
[44] A.B. Yousaf, M. Imran, P. Kasak, F.S. Zavahir, S.J. Zaidi, C. Fernandez, Catal. Sci. Technol. 7 (2017) 3283–3290.
[45] N.Y. Chen, M.C. Liu, S.C. Yang, J.R. Chang, J. Spectrosc. 2014 (2014) 347078.
[46] K. Sakaushi, S.J. Yang, T.P. Fellinger, M. Antonietti, J. Mater. Chem. A 3 (2015) 11720–11724.
[47] V. Cornette, J. Villarroel-Rocha, K. Sapag, R. Delgado Mons, J.P. Toso, R.H. López, Carbon 168 (2020) 508–514.
[48] M.H.M.T. Assumpção, R.M. Piasentin, P. Hammer, R.F.B. De Souza, G.S. Buzzo, M.C. Santos, E.V. Spinacé, A.O. Neto, J.C.M. Silva, Appl. Catal. B: Environ. 174–175 (2015) 136–144.
[49] L. Ma, D. Chu, R. Chen, Int. J. Hydrogen Energy 37 (2012) 11185–11194.
[50] L. Jiang, A. Hsu, D. Chu, R. Chen, Int. J. Hydrogen Energy 35 (2010) 365–372.
[51] H.Q. Pham, T.T. Huynh, T.M. Pham, V.T.T. Ho, Int. J. Hydrogen Energy 46 (2020) 16776–16786.
[52] D. Gubán, I. Borbáth, Z. Pászti, I. Sajó, E. Drotár, M. Hegedus, A. Tompos, Appl. Catal. B: Environ. 174–175 (2015) 455–470.
[53] F.J. Vidal-Iglesias, R.M. Arán-Ais, J. Solla-Gullón, E. Herrero, J.M. Feliu, ACS Catalysis 2 (2012) 901–910.
[54] S.L. Gojković, T.R. Vidaković, D.R. Durović, Electrochim. Acta 48 (24) (2003) 3607–3614.
[55] P. Waszczuk, H.S. Kim, Y.Y. Tong, A. Wieckowski, J. Solla-Gullón, V. Montiel, A. Aldaz, J. Catal. 203 (2001) 1–6.
[56] A. Santasalo-Aarnio, S. Tuomi, K. Jalkanen, K. Kontturi, T. Kallio, Electrochim. Acta 87 (2013) 730–738.
[57] H.X. Liu, N. Tian, M.P. Brandon, Z.Y. Zhou, J.L. Lin, C. Hardacre, W.F. Lin, S.G. Sun, ACS Catalysis 2 (2012) 708–715.
[58] Y. Lu, W. Wang, X. Chen, Y. Zhang, Y. Han, Y. Cheng, X.J. Chen, K. Liu, Y. Wang, Q. Zhang, S. Xie, Nano Res. 12 (2019) 651–657.
[59] E.G. Franco, A.O. Neto, M. Linardi, E. Aricó, J. Braz. Chem. Soc. 13 (2002) 516–521.
[60] F. Colmati Jr, W.H. Lizcano-Valbuena, G.A. Camara, E.A. Ticianelli, E.R. Gonzalez, J. Braz. Chem. Soc. 13 (2002) 474–482.
[61] E.V. Spinacé, A.O. Neto, M. Linardi, J. Power Sources 129 (2004) 121–126.
[62] L. Dong, Y. Wang, X. Tong, T. Lei, Diamond Relat. Mater. 104 (2020) 107739.
[63] Y. Fan, P.F. Liu, Z.J. Yang, T.W. Jiang, K.L. Yao, R. Han, X.X. Huo, Y.Y. Xiong, Electrochim. Acta 163 (2015) 140–148.
[64] H. Li, G. Sun, N. Li, S. Sun, D. Su, Q. Xin, J. Phys. Chem. C 111 (2007) 5605–5617.
[65] M. Watanabe, T. Mizukami, K. Tsurumi, T. Nakamura, P. Stoneharf, J. Electrochem. Soc. 141 (1994) 2659–2668.
[66] H.R. Colón-Mercado, B.N. Popov, J. Power Sources 155 (2006) 253–263.
[67] T. Iwasita, B. Rasch, E. Cattaneo, W. Vielstich, Electrochim. Acta 34 (1989) 1073–1079.
[68] M.H. Shao, R.R. Adzic, Electrochim. Acta 50 (2005) 2415–2422.
[69] F. Vigier, C. Coutanceau, F. Hahn, E.M. Belgsir, C. Lamy, J. Electroanal. Chem. 563 (2004) 81–89.
[70] N. Fujiwara, K.A. Friedrich, U. Stimming, J. Electroanal. Chem. 472 (1999) 120–125.
[71] Y. Hu, A. Zhu, Q. Zhang, Q. Liu, Int. J. Hydrogen Energy 41 (2016) 11359–11368.
[72] R. Ahmadi, M.K. Amini, J.C. Bennett, J. Catal. 292 (2012) 81–89.
[73] S. Lu, K. Eid, M. Lin, L. Wang, H. Wang, H. Gu, J. Mater. Chem. A 4 (2016) 10508–10513.
[74] H. Wang, Z. Jusys, R.J. Behm, J. Power Sources 154 (2006) 351–359.
[75] F.M. Sapountzi, M.N. Tsampas, H.O.A. Fredriksson, J.M. Gracia, J.W. Niemantsverdriet, Int. J. Hydrogen Energy 42 (2017) 10762–10774.
[76] B. Patil, B. Satilmis, T. Uyar, J. Power Sources 451 (2020) 227799.
[77] A. Paton-Carrero, A.R. de la Osa, P. Sanchez, A. Rodriguez-Gomez, A. Romero, J. Electroanal. Chem. 878 (2020) 114631.
[78] C.T. Hsieh, J.Y. Lin, J. Power Sources 188 (2009) 347–352.
[79] K.W. Park, J.H. Choi, B.K. Kwon, S.A. Lee, Y.E. Sung, H.Y. Ha, S.A. Hong, H. Kim, A. J. Phys. Chem. B 106 (2002) 1869-1877.
[80] J.E. Sulaiman, S. Zhu, Z. Xing, Q. Chang, M. Shao, ACS Catalysis 7 (2017) 5134–5141.
[81] D.Y. Chung, K.J. Lee, Y.E. Sung, J. Phys. Chem. C 120 (2016) 9028–9035.
[82] A.M. Hofstead-Duffy, D.J. Chen, S.G. Sun, Y.J. Tong, J. Mater. Chem 22 (2012) 5205–5208.
[83] I.A. Rutkowska, M.D. Koster, G.J. Blanchard, P.J. Kulesza, J. Power Sources 272 (2014) 681–688.
[84] I.A. Rutkowska, A. Wadas, P.J. Kulesza, Electrochim. Acta 210 (2016) 575–587.
[85] R.B. Kutz, B. Braunschweig, P. Mukherjee, R.L. Behrens, D.D. Dlott, A. Wieckowski, J. Catal. 278 (2011) 181–188.
[86] V. Rao, C. Cremers, U. Stimming, L. Cao, S. Sun, S. Yan, G. Sun, Q. Xin, J. Electrochem. Soc. 154 (2007) B1138–B1147.
[87] A.R. de la Osa, A.B. Calcerrada, J.L. Valverde, E.A. Baranova, A. de Lucas-Consuegra, Appl. Catal. B: Environ. 179 (2015) 276–284.